

Chapter 1

INTRODUCTION

1.0 Motivation, Objectives and Abstract

Motivation

Contemporarily, enormous efforts in developing CIGS thin-film are in progress. Subjugating challenges for developing and achieving high-efficiency records for CIGS solar cells and modules, a broad-range of various prospects of developing and commercializing the technology are still unraveled. Therefore, the rationale of understanding the fundamentals and developing the technology process is needed to improve and explore better clean and sustainable solar energy.

Objective

- To estimate the benefaction and utilization of renewable (Solar) energy resources.
- To achieve a better knowledge of the semiconductor mechanism of the photovoltaic device.
- To understand multilayer CIGS solar cell module consisting of Soda Lime Glass/ Mo/ CIGS/ CdS/ i-ZnO/ AZO functional layer profile with their properties for deposition utilizing the single-step sputtering and chemical bath deposition processes.
- To conceptualize LASER scribed monolithic integration from cell to module fabrication.

Abstract

Renewable energy is becoming entailed in human's day-to-day life's energy consumption. It gets replenished round-the-clock without contaminating the earth's atmosphere and gets easily converted into a usable form to meet the global energy demand. Solar energy is a notable form of renewable energy that is widely consumed globally. Photovoltaic cells and modules from silicon to quantum dot solar cell generation with a variety of chemical compositions have

demonstrated their capability, stability, and sustainability. In the present chapter, the production and consumption of solar energy and total world energy and are mentioned. How solar energy is distributed, as well as the performance of various photovoltaic cells and modules are described here. In this chapter, we elucidated all functional layers of the CIGS solar cell modules with stabilities and degradation properties.

1.1 Renewable resources – An Imperative Energy!

Renewable energy is currently an overriding area of interest where harvesting, production, and transformation of energy are important nodes of concern. Globally consumption of energy has escalated through technology, industries, residency, agriculture, usage etc. and it will keep constantly rising in the future also. Why there is a necessity for renewable energy? The answer is to negotiate with environmental, economic, and socially unsustainable non-renewable energy resources (natural oil, coal, natural gas, petroleum, fossil fuels). Compared to renewable resources, non-renewable energy resources have demerits such as they will be extinct soon, cost and efficiency of technology, a huge menace to the environment and can cause an ecological hazard, increment in carbon dioxide (CO₂) emission and highly unsustainable. Natural oil, coal, natural gas, petroleum, fossil fuels are non-renewable energy resources that will not replenish from their sources [1, 2] renewable energy resources. Renewable energy resources generate energy from solar power, wind power, wave, and tidal power, geothermal energy, and hydropower which have high sustainability, less CO₂ emission, and fewer hazards to the ecological environment. Among all renewable resources, solar power generated from the sun is the most preferred choice due to its availability all over the world at no cost. BP-Statistical Review World Energy estimates the world's total primary energy consumption in the year 2019 was 14378.0 Mtoe (Millions of oil equivalent) while production was 14715.0 Mtoe. Oil, natural gas, coal, nuclear energy, hydroelectricity, renewable energy are the drives contributing to total primary energy generation. Among them, sustainable, clean renewable energy shares 2805.0 TWh (Terawatt-hour) production of energy to total world energy production, and globally 28.98 exajoules are consumed in the year 2019 [3].

Human development and electricity consumption have a tight bond between them; all over the world total electricity generation capacity is 27004.7 TWh (Terawatt-hour) among which 26.67 % is contributed by renewable energy resources by the year 2019. The energy analysts report that the total world renewable energy capacity will increase to 50 % (approximately 1200 Gigawatts-total current capacity of the U.S). The world's cumulative total solar PV generation capacity and contribution of different renewable resources according to B.P statistics are shown in Fig. 1.1 (a and b). Solar energy can be easily harnessed by India in a huge amount due to its favorable geographical location. India ranked 5th in solar power installed capacity. In June 2019, India recorded an 80.46 GW capacity of renewable energy. This record was majorly summed up by 29.55 GW and 36.37 GW from solar and wind power, respectively. It is expected that the installed capacity of the solar power plant will exceed 100 GW by the year 2020 in India [4].

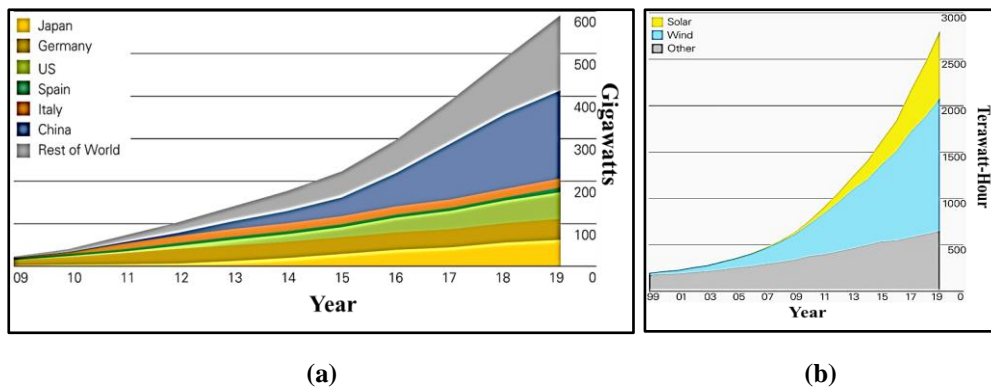


Fig.1.1: Solar PV generation capacity (gigawatts, cumulative installed capacity) and (b) Renewables generation by sources (terawatt-hours).

1.2 Solar Radiation Distribution

The Sun's photosphere has effective black body temperature (T_s) ~ 6000 K. Solar energy distribution in space is calculated using the below equation (1.1):

$$E = \varepsilon\sigma T_s^4 \quad (1.1)$$

Where ε and σ are the emissivity of the surface and Stefan's Boltzmann constant. The Earth's atmosphere contains greenhouse gases (GHG) like ozone (O_3), oxygen (O_2), nitrogen (N_2), carbon dioxide (CO_2), Carbon monoxide (CO), and water vapor (H_2O). This atmosphere transmits shorter wavelength radiation (0.23-2.26 μm) and opaque to higher wavelength radiation ($\lambda > 2.26$

μm). The solar spectrum has maximum fraction of energy in infrared region ($\lambda > 0.70 \mu\text{m}$) 53.12 % and 38.15 % visible region ($0.40 < \lambda < 0.70 \mu\text{m}$) and remaining 8.73 % in ultraviolet region ($\lambda < 0.40 \mu\text{m}$) [5]. This solar irradiance passes through the extraterrestrial and terrestrial region and due to greenhouse gases, there is ‘atmospheric attenuation’. The amount of ‘atmospheric attenuation’ is governed by ‘Air Mass’. The ratio of distance traveled by solar irradiance through the atmosphere to the mass traveled only when the Sun is at its Zenith angle (θ) shown in equation (1.2).

$$\text{Air Mass (AM)} = \sec\theta \quad (1.2)$$

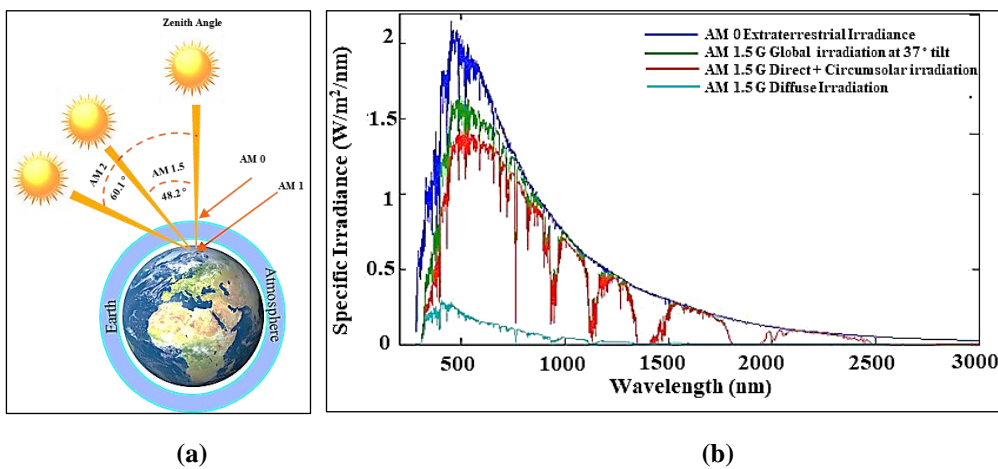


Fig.1.2: Spectral distribution of solar energy (a) at various zenith angle and (b) ASTM standard AM 1.5 G with different irradiation.

Air Mass ‘AM 0’ specifies that solar radiation has not interacted with the earth’s atmosphere (extraterrestrial region). Solar radiation distribution on the earth’s surface at different geographical locations, timings, and climatic conditions vary. The earth receives direct sunlight at the equator where solar radiation has to travel the least possible distance which is referred to as ‘AM 1’. The zenith angle (θ) varies with the geographical location points. At zenith angle 42.8° air mass increase to AM 1.5 and on further increment to 60.0° air mass become ‘AM 2’ shown in Fig. 1.2 (a). The standard solar irradiance spectra are accepted by the American Society for Testing and Material (ASTM) which are categorized as AM 1.5 Direct and AM 1.5 Global shown in Fig. 1.2 (b) [6]. AM 1.5 direct means only solar radiance directly from the sun’s surface and forward scattering around the sun’s surface i. e. ‘circumsolar’ normally to the flat surface (receiving device). ‘Global or total’ means solar radiation not only from the

direct sun's surface but also from 'diffuse radiation' from ground reflected radiation on a surface tilted at 37 ° from the horizon. These standards are widely accepted as testing standards for photovoltaic cells and collector's performance measurements. An increase in Air Mass indicates longer path length travel by solar radiation with more scattering and absorption due to atmospheric constituents such as aerosols, water vapor, and other air molecules. Dr. Christian. Gueymard (National Renewable Energy Laboratory, Colorado, USA) developed a Simple Model of Atmospheric Radiative Transfer of Sunshine 'SMARTS' using Fortran algorithms [7]. This SMARTS 2.9.2 model is used by researchers and engineers to measure spectral irradiance distribution on the clear sky day based on the American Society of Testing and Materials (ASTM) reference spectra (ASTM G-173 and ASTM G-177).

1.3 Photovoltaic-Generations and Performance

Antonie Cesar Becquerel developed solar technology in the year 1839. The first solar cell was made up of amorphous silicon developed by Chaplin, Fullere, and Pearson in the year 1954. Continuous increment in the demand of low cost, multivariant applicable hazard free and highly efficient solar cell provoked researchers to explore new emerging technologies for developing solar cells. Initially, only silicon technology has a monopoly over solar energy research and development as well as in electrification development [8]. Therefore, silicon technology is said to be the first generation of solar photovoltaic cells. Czochralski process float zone, Bridgman technique, Siemens process, and Pyrolysis process were used to develop Mono-crystalline and Poly-crystalline silicon solar cells [9, 10]. These processes give high conversion efficiency, but having demerits such as wastage of Si wafers, high probability defect formation in solar cell, and high processing cost. Mono-crystalline and Poly-crystalline silicon solar cells have achieved $26.7 \pm 0.5 \%$ and $22.3 \pm 0.4 \%$ solar conversion efficiency developed by Kaneka corporation and FhG-ISE respectively [11]. To overcome the demerits of the first-generation solar cell, a new innovative idea of reducing the thickness of the active or absorber layer has boomed out. Cadmium Telluride (CdTe), Copper Indium Gallium Diselenide (CIGS), Amorphous silicon (a-Si), and Gallium Arsenide (GaAs) have proven

themselves as prominent choices of absorber layer to develop solar photovoltaic cells. These solar cells are known as second-generation solar photovoltaic cells [12]. Their thickness ranges from 0.1 μm to less than or equal to 1 μm . Thermal evaporation, RF sputtering, DC sputtering, Co-evaporation technique, Metal-Organic Chemical Vapor Deposition (MOCVD), Molecular Beam Epitaxy (MBE), etc. are the deposition techniques used in developing second-generation solar photovoltaic cell [13-16]. A remarkable world record has been noted in the ALTA device on account of GaAs thin-film solar cell $29.1 \pm 0.6 \%$ efficiency. Solar Frontier has marked $22.9 \pm 0.5 \%$ efficiency on CIGS solar cells of the 1 cm^2 area. Single Junction terrestrial CdTe solar cell on glass substrate developed by First Solar has achieved an efficiency of 21.0 % [17-19]. Researchers at the National Institute of Advanced Industrial Science and Technology, Tokyo, Japan have developed a-Si and micro-crystalline cells having solar conversion efficiency of about $10.2 \pm 0.3 \%$ and $11.9 \pm 0.3 \%$. Miasole has developed a CIGS solar panel of 1 m^2 with $18.6 \pm 0.6 \%$ solar conversion efficiency [20]. The disadvantage of second-generation solar cells for industrial production is the unavailability of less abundant elements like Te, Cd, Ga, In, etc. Also, elements like Te and Cd are highly toxic and hazardous to human health [21]. To date, mass production of the second-generation solar cell is not affordable and adaptable in terms of the high cost of material, manufacturing, and installation of solar panels. To reduce the toxicity of chemical elements, Third Generation solar cell has come up with Dye-sensitized solar cells (DSSC), Organic/Polymer Photovoltaic cells, and Copper Zinc Tin Sulphide (CZTS) solar cells [22, 23]. One of the major advantages of the third-generation solar cell is having low manufacturing costs. Third-generation solar cells are manufactured by the roll to roll printing, screen printing, and other vacuum and non-vacuum techniques [24, 25]. Sharp Corporation has fabricated DSSC with a single solar cell, a mini-module of 7 serial cells, and a sub-module of 26 serial cells with an efficiency of $11.9 \pm 0.4 \%$, $10.7 \pm 0.4 \%$, and $8.8 \pm 0.3 \%$, respectively. These organic dyes can generate electricity through illumination in electrochemical cells [26]. Researchers at the University of South Wales, Australia, have reported that the heterojunction heat treatment process of CZTS solar cell improves the performance due to the inter-diffusion of elements and lead to solar efficiency of 11 % for small area cells (0.23 cm^2)

and 10 % for a standard-sized cell (1.11 cm^2) [27]. Toshiba has developed organic solar cells and a minimodule of series of 8 cells with solar efficiency of $11.2 \pm 0.3 \%$ and $9.7 \pm 0.3 \%$, respectively [28]. To enhance the performance, stability, and efficiency of solar cell multiple junction solar cells with broad spectral absorber wavelength have been developed. Multijunction solar cells such as GaInP/GaAs/Si monolithic ($22.3 \pm 0.8 \%$), Perovskite/Si monolithic ($27.3 \pm 0.8 \%$), InGaP/GaAs/InGaAs ($31.2 \pm 1.2 \%$) are about to reach Shockley-Quiesser limit (33 %) [29]. Well apart from the above-mentioned efficiency records, performance reports of various multijunction cells, single-junction GaAs, crystalline Si cells, thin-film technologies (cells and concentrators), and emerging PV technology over decades have been shown in Fig. 1.3.

1.4 Fundamentals of Photovoltaic Device

The photovoltaic device works on the conversion of solar energy into electric energy using the ‘photoelectric effect’. For this conversion of energy, the layer must absorb solar radiation and further it should create mobile charge carrier electron and hole pairs and they should be individually collected at the terminals. Bandgap energy (E_g) of an absorber layer is the most prime important factor to analyze the conversion efficiency performance of the solar cells. After light absorption with energy ‘E’, conduction and valence band edges get thermalize and the generated energy per absorbed photon is the bandgap ‘ E_g ’ of the material (absorber layer). Bandgap quantifies the amount of generation of electron and hole pair generated from a solar cell with energy $E \geq E_g$. Shockley and Quiesser derived ‘Detailed -Balanced limit’ also known as S-Q Limit for maximum power conversion efficiency of a solar cell having a single absorber layer. This limit is based on four assumptions: (1) light absorption probability by the generation of single-electron-hole pair is unity for all photons with energies E when $E \geq E_g$ and zero for $E < E_g$. (2) All photogenerated charge carriers can thermalize at the band-edges. (3) In a short-circuit current the collection probability of generated charge carriers is unity. (4) The loss mechanism of excessive non-absorbed photons is thermalization loss and spontaneous emission of photons by radiative recombination. To evaluate the

performance of the solar cells four parameters is considered, (1) Short circuit current density (J_{sc}), (2) Open circuit voltage (V_{oc}), (3) Fill-Factor (FF), and (4) carriers can thermalize at the band-edges. (3) In a short-circuit current the collection probability of generated charge carriers is unity. (4) The loss mechanism of excessive non-absorbed photons is thermalization loss and spontaneous emission of photons by radiative recombination. To evaluate the performance of the solar cells four parameters are considered, (1) Short circuit current density (J_{sc}), (2) Open circuit voltage (V_{oc}), (3) Fill-Factor (FF), and (4) Quantum Efficiency (η %). For an applied voltage ($V = 0$ V), the incoming photons flux (ϕ_{inc}) and absorptance $A(E)$ defines the percentage of photon energies that are absorbed not reflected or transmitted. Based on Shockley and Quisser assumptions short circuit current $J_{sc, SQ}$ is calculated using the following equation (1.3) [30]:

$$J_{sc,SQ} = q \int_{E_g}^{\infty} \phi_{inc}(E) dE \quad (1.3)$$

Short circuit current is not only generated from free charge carrier, but also the light emission by recombination of electron-hole pairs. According to detailed balance theory, in thermodynamical equilibrium condition the emissivity ϕ_{em} is interrelated with absorptance via Kirchhoff's law, $\phi_{em} = A(E)\phi_{bb}(E, T)$, where $\phi_{bb}(E, T)$ is the black body spectrum at temperature T. Using Wurfel's generalization of Kirchhoff's law, recombination current due to radiative recombination $J_{rec,SQ}$ can be evaluated as following equation (1.4):

$$J_{rec,SQ} = q \int_{E_g}^{\infty} \phi_{bb}(E, T) \exp\left(\frac{qV}{kT}\right) dE \quad (1.4)$$

The total current density $J(V)$ under the illumination expressed in equation (1.5) as a combination of short circuit current density $J_{sc, SQ}$ and radiative recombination current density $J_{rec, SQ}$;

$$J(V) = J_{rec,SQ} - J_{sc,SQ} = q \int_{E_g}^{\infty} \phi_{bb}(E, T) \exp\left(\frac{qV}{kT}\right) dE - q \int_{E_g}^{\infty} \phi_{inc}(E) dE \quad (1.5)$$

Under open circuit condition $J = 0$, the fourth quadrant of the coordinated system has maximum possible voltage; this voltage refers to Open circuit voltage V_{oc} as shown in equation (1.6):

$$V_{oc} = \frac{kT}{q} \ln\left(\frac{J_{sc,SQ}}{J_{0,SQ}} + 1\right) \quad (1.6)$$

$J_{0,SQ}$ is the saturation current density in SQ-limit. The open-circuit voltage increases linearly with an increase in the bandgap. According to thermodynamic reasoning, the J/V curve takes the following equation (1.7) form:

$$J = J_0 \left[\exp\left(\frac{qV}{kT}\right) - 1 \right] - J_{sc} \quad (1.7)$$

Where J_0 is the saturation current, J_{sc} is short circuit current and $\frac{kT}{q}$ is the thermal voltage. The recombination rate is directly proportional to electron (n) and hole (p) concentrations ($R \propto np$). These charge carriers have high mobilities and assuming $np = n_i^2 \exp\left(\frac{qV}{kT}\right)$. Therefore, recombination current density J_{rec} is equal to the dark current density J_d described in the following equation (1.8):

$$J_{rec} = J_d = J_0 \left[\exp\left(\frac{qV}{kT}\right) - 1 \right] \quad (1.8)$$

In a thin-film solar cell, the recombination mechanism is Shockley-Read-Hall recombination via defects in the bandgap. Assuming the presence of defects in the middle of the bandgap, recombination will be following equation (1.9):

$$R = (n = P) = \frac{np - n_i^2}{(n+p)\tau} \approx \frac{n}{2\tau} = \frac{\sqrt{np}}{2\tau} \quad (1.9)$$

Where ‘ τ ’ is the lifetime of electrons and hole and it is equal for both. The type of recombination is dependent on the higher or lower voltage. If the voltage is high, then recombination takes in the bulk or at the absorber surface away from the space charge region. In the case of low voltage, the space charge region has recombination where the concentration of electrons and holes change in the region. The concentration product ‘ np ’ is directly proportional to $\exp\left(\frac{qV}{kT}\right)$, V is the internal voltage of the quasi-Fermi level splitting. Then recombination will take form as the following equation (1.10):

$$R (n = p) \propto \sqrt{\exp\left(\frac{qV}{kT}\right)'} = \exp\left(\frac{qV}{2kT}\right) \quad (1.10)$$

$\frac{q}{2kT}$ is the recombination current. The factor ‘2’ is the ideality factor or diode quality factor ‘ n_{id} ’. For higher voltage, the value is around ‘1’ and for low voltage it near but less than ‘2’. Theoretically, the ideality factor is in range $1 < n_{id} < 2$ which is dependent on the energy of the recombination center and capture cross-section for electrons and holes. The $n_{id} > 2$ is difficult to explain but it is possible due to multiple-step recombination via series of trap states

distributes in space and energy is acquired by recombination in the space-charge region. The Fill-Factor is the largest rectangle that fits between J/V curve and the axis is divided by the rectangle with $V_{oc} J_{sc}$ mentioned in the equation (1.11) below:

$$\text{Fill Factor (FF)} = \frac{P_{mpp}}{V_{oc} * J_{sc}} \quad (1.11)$$

Where P_{mpp} is the maximum power density of the photovoltaic device. Reduction in fill-factor is due to the incapability of the device to collect charge carrier under forward bias condition. Here the built-in field is reduced.

The conversion efficiency of photovoltaic devices is defined in the following equation (1.12):

$$\eta (\%) = \frac{V_{oc} J_{sc} FF}{P_{in}} \quad (1.12)$$

Where P_{in} is the total input power of incident light on the photovoltaic device. In a real solar cell, the Shockley-Queisser limit has limitations due to recombination losses therefore efficiency is termed as External quantum efficiency and internal quantum efficiency. The External quantum efficiency ' Q_e ' is the number of electrons collected per incident photon according to the below equation (1.13):

$$Q_e (E) = \frac{1}{q} \frac{dJ_{sc}(E)}{d\Phi(E)} \quad (1.13)$$

Here, $d\Phi(E)$ is the incident photon flux [unit of $\Phi = (\text{cm}^{-1} \text{s}^{-1})$] in the interval of energy (dE). The internal quantum efficiency is function optical and recombination losses. But major contribution is from an optical loss such as parasitic absorption and reflection. When all photon is not reflected, they are absorbed in device giving rise to internal quantum efficiency Q_{in} . It is termed as the number of collected electrons per absorbed photon in the solar cell defined as the following equation (1.14):

$$Q_{in} = \frac{Q_e}{1-R(E)} \quad (1.14)$$

Where 'R' is the reflectance. For thin layers, especially for the absorber layer, the denominator can be replaced by absorption ' A_i '.

1.5 Profile of Chalcopyrite CIGS Solar Cell Module

Copper Indium Gallium Diselenide (CIGS) is a quaternary chalcopyrite compound. CIGS solar cell module is a second-generation thin-film photovoltaic device. This compound belongs to $CuB^{III}C_2^{VI}(B^{III} = Ga, In; C_2^{VI} = Se, S)$ group. Tailoring the band gap between ternary $CuInSe_2$ (1.01 eV) and $CuGaSe_2$ (1.72 eV) compound with substitution of Ga into sites of In atoms i.e. $(Cu In_{1-x} Ga_x Se_2; 0 < X < 1)$ is adopted for achieving high performance of solar cell module. In the present work, we have substituted $X=0.3$; this attributes CIGS having a high absorption coefficient ($\alpha \sim 10^5 \text{ cm}^{-1}$), direct bandgap (1.15 eV), long-term stability, and with long diffusion length. CIGS solar cell module embraces a stack of multilayer Mo/CIGS/CdS/i-ZnO/AZnO on a substrate. The multilayer was formed by using various deposition techniques like DC sputtering, RF sputtering, Chemical Bath Deposition, and Thermal Evaporation. Each layer has its own key role in the performance of the CIGS solar cell module. Here p-n junction is formed by the p-type CIGS layer and n-type CdS layer. For module fabrication, CIGS solar cells are integrated into arrays i.e., monolithic interconnection using a laser scribing process. The schematic of the CIGS solar module using the laser scribing process is shown in Fig. 1.4. A brief introduction of each layer is mentioned below:

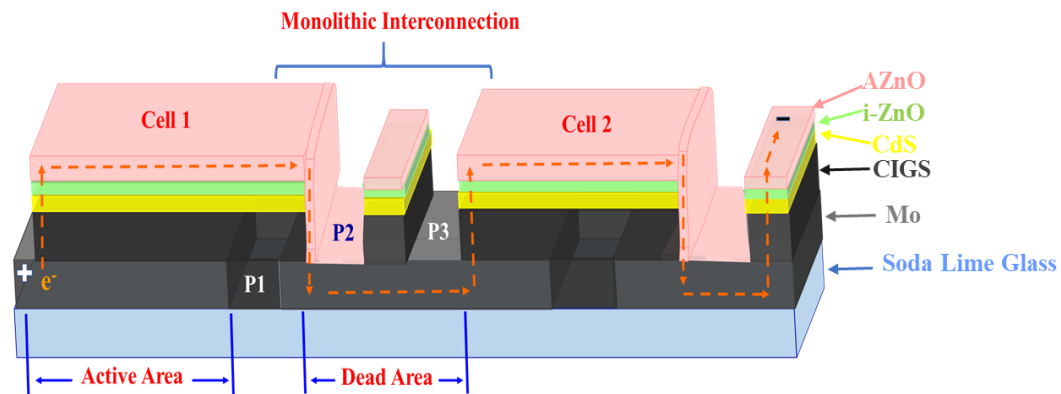


Fig. 1.4: Schematic of CIGS Solar cell module using a laser scribing process.

1.5.1 Substrate

The substrate is the cornerstone of photovoltaic device performance and stability. Substrate focus on thermal expansion, chemistry, and surface influence on the nucleation of functional layers deposited over it. Two prime

features of the substrate are to provide mechanical and thermal stability. Even they should be tensile stress-free for high adhesion quality of the functional layer. A wide range of substrates has been used for CIGS solar cell devices. The most preferred low cost, rigid substrate is soda-lime glass (SLG). It has a $9 \times 10^{-6} \text{ k}^{-1}$ coefficient of thermal expansion and can withstand up to $600 \text{ }^\circ\text{C}$ for a further high-temperature fabrication process. CIGS solar cell has shown progressive performance with flexible, lightweight, and low-cost substrate. Foils or ribbons of stainless steel, copper, mild steel, titanium, nickel/iron alloy, molybdenum, and aluminum have been used as a flexible substrate [31]. They have a thermal coefficient of expansion ranged from 4.8×10^{-6} - $23 \times 10^{-6} \text{ k}^{-1}$. The ceramic substrate of zirconium oxide and polyamide substrates like Kapton tape and polyethylene terephthalate (PET) are popularly used as substrate.

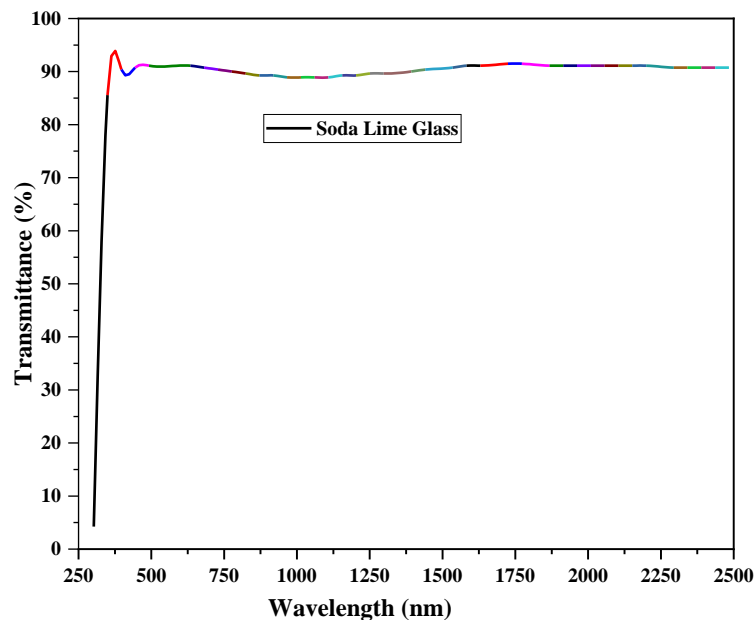


Fig. 1.5: Transmittance spectra of substrate-Soda Lime Glass (Marienfeld, Germany)

In the present fabrication process, the soda-lime glass substrate was procured from Marienfeld, Germany. The transmittance spectra of $60 \times 60 \times 1 \text{ mm}$ soda-lime glass substrate is shown in Fig. 1.5. Not only the optical but physical properties and chemical composition of substrate significantly affect the performance of the photovoltaic device. For the CIGS solar cell module, processing temperature ($\sim 550 \text{ }^\circ\text{C}$), diffusion of sodium (Na), and hardness of the substrate are a few primary requirements. The soda-lime glass substrate which has been used in the fabrication is capable to fulfill all primary

requirements. Table 1.1 describes the physical properties and chemical compositions of soda-lime glass (Marienfeld, Germany)

Table 1.1: Physical properties and Chemical composition of Soda-lime glass.

Physical Properties of Soda Lime Glass	
Transmission: TL (Auge*D65) for glass thicknesses of 1mm	TL = 91.2 % ± 1%
Refractive index	(N _{ad}) = 1.52
Density	2.5 x 10 ³ kg/m ³
Coefficient of thermal expansion	α = 9 x 10 ⁻⁶ K ⁻¹ at 20-300 °C
E modulus	7.3 x 10 ⁴ N/mm ²
Poissons ratio	0.23
Vickers hardness	5 x 10 ³ N/mm ²
Resistance to pressure	700 – 900 N/ mm ²
Transformation temperature	Log η =12.3; T~567 °C
Annealing point	Log η =13.0; T~557 °C
Dilatometric start of softening	Log η =10.3; T~598 °C
Softening point: (η=viscosity in Pa.s)	Log η =7.6; T~726 °C
Alkaline resistance (ISO 695)	Class 1-2
Acid resistance (ISO 8424)	Class 1
Hydrolytic resistance (ISO 719)	Class 3
Chemical Compositions	
SiO ₂	72.3 %
Na ₂ O	13.4 %
CaO	8.8 %
MgO	4.2 %
Al ₂ O ₃	0.5 %
K ₂ O	0.4 %
SO ₃	0.3 %
Fe ₂ O ₃	<= 0.05 %

1.5.2 Back contact layer

In the present work, a configuration of a solar cell module, the back-contact layer is the first layer deposited on a substrate. The back-contact layer is ‘ohmic’ in nature. This ohmic back contact is required to drive current towards the external load. An interface between photovoltaic active (absorber) and back contact layer forms metal-semiconductor contact which is essential for minimizing losses in the solar cell module. The ratio of the voltage drop across an ohmic contact and current flowing through it is termed as ‘contact resistance’; for good ohmic contact, the value of contact resistance should be

low. Both the Fermi energy level of the ohmic contact layer is positioned with Fermi energy levels of the absorber layer. Ohmic contact does not instigate the formation potential barrier to mobile electrons and holes, this layer is not a charge selective layer. Ohmic back contact's pivotal features are lowest sheet resistance ($< 0.332 \Omega/\square$), high reflectivity, chemically inert, highly adhere, and good mechanical stability with a matching coefficient of thermal expansion with the substrate. Refractory metals like Cu, Ag, Au, Pt, Mo, Al, and Ni are one the prominent choice for ohmic back contact. Among these, Mo is widely used as it possesses all necessary features for good ohmic back contact so that it can have good light trapping and easily reflect weakly absorbed light and boost the charge extraction process. At the interface between back contact and the absorber layer, a layer has formed (e. g. MoSe₂ layer) as ohmic in nature which promotes conductivity and adherence with the absorber layer.

1.5.3 Absorber layer

The absorber layer has been attributed to the photovoltaic conversion process. The main aim of this layer is to absorb light, generation of electron-hole pair, and charge extraction. For high conversion efficiency, it should have a high absorption coefficient, high mobility of free charge carriers, and low recombination rates of electrons and holes. At metal (back contact)-semiconductor (absorber layer) interface ohmic contacts are not charge selective whereas semiconductor (absorber layer)-semiconductor (buffer layer) is charge selective. An absorber layer forms a p-n junction with a buffer layer where incident photons modify Fermi-energy of the minority carrier and due to which photovoltage is generated. A route to achieve high efficiency is to reduce the optical and resistive losses due to recombination at the absorber-buffer interface. Adding Gallium to ternary compound Copper Indium Selenide (CIS), a chalcopyrite structure Copper Indium Gallium Diselenide (CIGS) has formed with tunable direct bandgap due to addition and variation in Gallium composition. This compound belongs to $CuB^{III}C_2^{VI}(B^{III} = Ga, In; C_2^{VI} = Se, S)$ group possessing a tetragonal crystal structure. Tailoring the band gap between ternary CuInSe₂ (1.01 eV) and CuGaSe₂ (1.72 eV) compound with substitution of Ga into sites of In atoms i.e. (Cu In_{1-x} Ga_x Se₂; $0 < X < 1$) has

adopted for achieving high performance of solar cell module [32]. In the present work, we have substituted $X=0.3$; this attributes CIGS having a high absorption coefficient ($\alpha \sim 10^5 \text{ cm}^{-1}$), direct bandgap (1.15 eV), long-term stability, and with long diffusion length. For highly efficient device, the preferred stoichiometric composition $\text{Cu}/(\text{In} + \text{Ga}) = 0.9\text{-}1.0$, $\text{Ga}/(\text{Ga} + \text{In}) = 0.3$ and $\text{Se}/(\text{Cu} + \text{In} + \text{Ga}) = 1.0$. Although slight Cu-deficient is more preferred due to the availability of Cu-vacancy to act CIGS as a p-type absorber. Self-Compensating neutral defects ($2V_{\text{Cu}}^- - \text{In}_{\text{Cu}}^{2+}$) pair will contribute to net doping resulting in slight Cu deficiency. This helps to improve the efficiency of CIGS solar cells. Deviation in a stoichiometric composition may be due to the formation of defects or other phases like CuSe, Cu₂Se, In₂Se₃, β -(In, Ga)₂Se₃, or Ga₂Se₃. Although these defects and recombination of photogenerated carriers hinder the performance of CIGS solar cells. Recombination takes place in the quasi-neutral region, space charge region, interface, and surface. The charge transport mechanisms have to face challenges like barrier formation at the interface or deep level traps at the bulk region. There are discontinuities in band-alignment at the interface due to offsets in valence band maximum (ΔE_{VB}) and the conduction band minimum (ΔE_{CB}). Due to the presence of heteronuclear chemical interface bonds, at interface charge gets transfer into electronic states localized forming interface dipoles. The band alignment between absorber and buffer layer should be type-I and ΔE_{VB} and ΔE_{CB} value should be smaller than the band-gap difference of both layers. The absorber layer possesses a grain boundary during growth-mechanism with a different configuration like charge-free horizontal and columnar, majority hole-repulsive band bending, minority electron-repulsive band bending, downshift in valence-band energy and there may be the possibility of a combination of above configurations also. This grain boundary affects the performance of the solar cell [33, 34]. For improving performance (V_{oc} , FF, and efficiency), undergoes post-deposition treatment (PDT) such as Rapid thermal annealing with doping alkali fluoride (Na, K, Cs, and Rb). PDT treatment passivates defects at the absorber layer's surface and grain boundary. This lowers the Fermi level (E_{F}) due to an increase in p-type carrier concentration and turns enlarged differential E_{F} helps to improve V_{oc} .

1.5.4 Buffer layer

A buffer layer is the heterojunction partner of an absorber layer forming the p-n junction. The buffer layer has the responsibility to provide high transmission of incoming photons to the absorber layer by having a wide-bandgap for minimum absorption loss to the absorber layer, least lattice-mismatch of highly oriented crystal with absorber layer to take the edge off the interface defects, band alignment should have optimum band-discontinuities without band-offsets and doping densities in buffer layer should be high compare to absorber layer to suppress the interface recombination due to minority charge carrier and form interface states [35, 36]. In case of the presence of a band-offset for minority charge carriers, then 'spike' is more preferred compare to 'cliff' to decrease the probability of interface cross-recombination process. The buffer layer also functions as surface cleaning and passivates the surface of the absorber layer. For the buffer layer, heavy metal sulfides, binary sulfides, and oxy-sulfides are the prominent choices (CdS, ZnS, ZnS (OOH), ZnSe, In₂Se₃, Zn_{1-x}Sn_xO_y, etc.) [37]. Cadmium Sulphide (CdS) serves as an n-type buffer layer having a hexagonal phase structure. It has a direct wide gap (2.4 eV), low electrical resistivity, and high visible transparency. It protects the absorber layer from the incoming sputter ions of the window layer optimum thickness of the CdS layer passivates the absorber layer, high doping concentration form n-type near the interface, and form buried homojunction which enhances the performance of CIGS solar cell.

1.5.5 Window layer

The window layer is the top electrode layer of solar cells deposited on the buffer layer. The role of the window layer is to provide high transmission at higher wavelength, low resistivity, and good front contact to collect lateral charges [38]. To meet this requirement, the window layer should have a wide bandgap, transparent, highly conductive, low toxicity, and cost. For this, transparent conductive oxide (TCO) (doped) material is recommended to be used as a window layer. The bilayer of (i-ZnO) intrinsic-Zinc Oxide (undoped) and (AZO) Aluminum doped Zinc Oxide (doped) is often used. AZO has a wide direct bandgap (3.34 eV), low sheet resistance ($< 9 \Omega/\square$), high electron mobility,

and highly transparent ($> 90\%$) in the visible region makes it a promising candidate for the window layer. It has a hexagonal phase structure, but to reduce the lattice mismatch between the buffer window layer, a highly resistive i-ZnO layer of approximately 50-70 nm thickness is deposited. This layer not only reduces the lattice mismatch but also provides shunt resistance to lower the effect of short circuit pathways due to the presence of pinholes in the buffer layer. The optimum thickness of the i-ZnO layer affects the V_{oc} of the solar cell; low thickness will have high band discontinuities whereas too thick will weaken the built-in field by spreading the space-charge region over thickness. In fabricating solar cell modules, the AZO layer forms a junction and interconnects with another cell in the module.

1.5.6 Monolithic Integration: Cell to Module

To achieve the desired V_{oc} cells need to be connected in combination with series and parallel network. Traditionally, a hand-cut or machine wire cut process was widely used for interconnection. Tabbing string and ribbons or using soldering or using an electrically conductive adhesive, shingle overlap or wire overlay, and grid aided monolithic interconnection methods were adapted for mass production. But there were limitations like delamination due to difference in thermal coefficient of string and solar cell, equipment and process cost, string material consumption, and highly resistive losses. The alternative method ‘scribing’ of layers during the fabrication of cells to the module was adopted. Scribing means ‘selective ablation’ or ‘isolating/patterning’ layer by cleaving them or by lift-off technique. In monolithic integration of the CIGS solar cell module, three times the scribing process at a different level of fabrication process must be carried out [39]. At the first scribing step, isolation of the bottom electrode i. e., conductive ohmic back contact has been done. The second scribing step is performed on the stack of the p-n junction semiconductor layer keeping the first layer intact to the substrate. This process refers to the ‘lift-off’ process. At this step, the interconnection path between cells has formed. Finally, at the third step above the top electrode i.e., window layer scribing process has been done to connect the top electrode of one cell to the bottom electrode of another cell in a series network. In this way, all cells in the

module are isolated. To lower the series resistance, the residues of the p-n junction or window layer should be negligible. The probability of forming a 'bridge or channel' between the top and bottom electrode layers is there in case of failure to complete isolation or residual of material. This will lead to shunting in the device and deteriorate the performance of the module. Two techniques were used for the scribing process, one is mechanical and another with the help of a laser. The 'Mechanical scribing' process was a cost-effective process in which a diamond or tungsten tip/blade was used to isolate the layers. Mechanical fracture, burrs, shunt path, cost of a tip, and repeatability issues were noted. To overcome these issues, the 'laser scribing' process was introduced. Depending upon the optical and physical properties of materials used in the fabrication of the module, the type of laser, and its working parameters such as power, pulse repetition rate, scribing speed, pass delay, and depth of focus need to be chosen. Here we used Nd:YAG 1064 nm nanosecond laser and two different optical setups, first using YAG focusing lens and second YAG f-theta lens with Galvo mirror for the scribing process. Hence, laser scribing is a robust, high speed, non-contact, clean, burr-free, less heat affected zone area (HAZ) process.

1.6 Stabilities, Band-alignment, and Degradation

Improvement in efficiency, formation, and stabilities of defects, long term duration capabilities, and degradation are the key aspects where the module must justify its performance. Being a multi-layer device, CIGS solar cell module comprises of Mo, Cu, In, Ga, Se, Cd, S, Al, Zn, and O elements. Also, there is a possibility of Na diffusion from the glass substrate or due to post-deposition treatment. The presence of the above elements confirms the complexity of solid-state chemistry in the module at bulk and interface region; electronic properties of the module will also get modify on illumination, applying bias, or on storage of charge in the dark region. CIGS solar cell consists of Mo/CIGS, CIGS/CdS, CdS/i-ZnO, and i-ZnO/AZO interface, and stability is affected by the interfacial reaction. At Mo/CIGS interface, the MoSe₂ layer is formed in the presence of excess Se which is the beneficial photovoltaic quality of the film. No Mo diffusion in the CIGS layer has been reported yet.

CIGS/CdS interface possesses a high probability of interface recombination centers. The solution prepared for CdS helps to remove the secondary phases and reduce surface recombination. The performance of the CIGS device is based on electrical stability depending on short-range and long-range mechanisms in the device. According to findings [40] short-range and long-range mechanisms are classified as illumination-induced metastability and bias-induced metastability in the absorber (CIGS) layer. CIGS is found to be non-degenerate for doping concentration on composition changes. This fact proves the strong self-compensation nature of CIGS material. Deviation from stoichiometry results in the formation of defects and defect complex having shallow energy level or outside the bandgap and they must be electronically inactive concerning surface recombination. $(2V_{Cu}, In_{Cu})$ is a most stable and neutral complex found on In rich side whereas neutral defect complex like $(2Cu, Cu_{In})$ was found due to large energy formation. Defects are present in both stable at absolute minimum energy as well as in metastable local minimum energy position. CIGS manifest metastable reaction with intrinsic defects and these defects are performance enhancers rather than degraders and the most important feature is that they all are reversible at room temperature. In the metastable state, defect reaction occurs due to electron-lattice coupling which is probably due to the re-arrangement of an isolated point defect or defect-defect interaction. Therefore, either there could be a charge state of donor defect or defect-defect reaction in which there is the conversion of donors to acceptors. E. g. $(In_{Cu})^{++}$ converts to In_{Cu} (neutral) or $(In_{Cu}, Cu_{In})^{++}$ to (In_{Cu}, Cu_{In}) . Cu interstitial Cu_i and Cu vacancy V_{Cu} , Cu_{In} are easily found in the absorber layer. The buffer layer also possesses metastability in terms of ‘Kink’ which is reflected in the I-V curve. ‘Kink’ represents the potential drop across the buffer layer; insufficient electron density forms an effective barrier for electron transportation. To reduce ‘kink’ blue light generates a hole and firmly capture in the acceptor state and there is an increase in net donor electron density which increases potential across it. Changes in copper concentration were effectively observed under the influence of mild bias, temperature, and illumination exposure. Electric bias affects the change in position of Fermi level due to which Cu vacancies are increased which in turn decreases Cu concentration. Alteration of doping profile in the CIGS

layer is more pronounced with an increase in temperature (during post-deposition annealing or rapid thermal annealing) and longer bias time. But the restoration of the doping profile was observed for the mild dosage of bias or temperature under resumed circumstances. Similarly, a combination of electric forward bias and illumination induces photo-bias to modify the dopant profile by increasing overall hole density. Thus, the CIGS layer possesses two important features: 1. availability of large pool defects and 2. migrations of ions. The feature does not degrade the performance of CIGS solar cell devices instead they are beneficial as they increase effective doping. Especially, Cu ions migration passivates the defect present in the absorber CIGS layer, because defects have very enough low formation of energy so that they can be passivated at room temperature also. Therefore, CIGS is considered a flexible, smart, and dynamic absorber layer. Band alignment of the stack of layers in a photovoltaic device is the blueprint of its performance. Innate band alignment is theoretically predicted but pragmatically fabricated photovoltaic device comprised of lattice mismatch, defects centers in bulk as well as at interface. This reduces the performance of the device compared to predicted ones. Anderson's rule based on the electron-affinity of material is used to predict the band-alignment. 'Cliff' or 'Spike' in the conduction band or valence band at the interface or bulk region of the layer depicts the transport route of extracted charge carriers across the device. It is inferred that 'spike' at CIGS/CdS conduction band offers better performance but 'cliff' with conduction band offset less than 0.5 eV acts as a barrier for minority carrier transportation. Few literature surveys on band alignment adaptation due to various deposition parameters in CIGS solar cell device is mentioned here. Fig. 1.6 (1) represents the standard band alignment diagram of the CIGS solar cell device having a positive 'cliff'. Recombination at bulk CIGS layer, space charge region (SCR), and at CIGS/CdS are probable here [41]. A. O. Pudov et. al., has performed a numerical simulation using AMPS-1D software. They found a 'cliff' in band alignment when illumination with red (without blue photons) and white (with blue photons) light shown in Fig. 1.6 (2 and 3) causing band alignment modification with increasing gallium concentration. He also simulated with different CdS thickness i. e. 75 nm in Fig. 1.6 (6) and 25 nm in Fig. 1.6 (7) under illumination with blue photons. As a result, a reduction in the secondary barrier was predicted for both thicknesses

[42]. Post Deposition Treatment (PDT) of alkali-fluoride (NaF in Fig. 1.6 (4) and NaF + KF in Fig. 1.6 (5)) under the selenium atmosphere improve the open-circuit voltage of CIGS solar cell device [43]. The valence band of NaF + KF PDT stretched down compared to NaF PDT due to a decrease in hole concentration and thus recombination at the interface is also reduced while improving the efficiency of the device. O. Lundberg et. al. [44] suggested the importance of normal and double Ga-grading shown in Fig. 1.6 (8) with standard and reduced thickness i.e. (1.5-2.0 and 0.5 μm). He concluded that reduced thickness of CIGS with Ga grading towards back contact improves open circuit and fill factor due to the passivation of the CIGS layer and further adds that Ga-grading at the front part i. e. towards the CdS layer did not show any significant performance improvement. Using SCAPS simulation software, Fredrik. Larson et. al. demonstrated band alignment of CIGS device having an intrinsic-Zinc oxide layer of thickness 20 nm shown in Fig. 1.6 (9) [45] and 160 nm in Fig. 1.6 (10) with a high donor carrier concentration of order 10^{17} cm^{-3} . Inversion at CIGS/CdS for both thin and thick layers as well as proportional open circuit voltage was observed. Open circuit voltage is independent of i-ZnO thickness if carrier concentration is high enough. An attempt had been made by Giovanna. Sozzi to understand field-effect passivation over point contact geometry or complete coverage of the passivation layer over nanopatterned will boost the performance of CIGS device [46]. He simulated band alignment by fixing positive charge density $Q_f = 0, 10^{12} \text{ cm}^{-3}$ and presence of defects as an acceptor trap density $N_{AT} = 10^{11} \text{ cm}^{-3}$ and $V = 0.4 \text{ V}$ at maximum power point. The inimical effect of acceptor trap density at CIGS/CdS front point contact geometry and all over the absorber layer was examined. He concluded that positive Q_f added field-effect passivation which reduces the barrier so that photo-generated electron move-in buffer layer. This also promotes electron accumulation forming an inverted passivated/absorber layer interface. This reduces the resistance of the current path inside the absorber layer and thus improves the fill factor. The impact of field passivation for $Q_f = 0 \text{ cm}^{-3}$ in Fig. 1.6 (11), $Q_f = 10^{12} \text{ cm}^{-3}$ in Fig. 1.6 (12) for front side point contact geometry and $Q_f = 0$ in Fig. 1.6 (13) and $Q_f = 10^{12} \text{ cm}^{-3}$ in Fig. 1.6 (14) for complete passivated are over nanopatterned CIGS layer is shown. This field-effect passivation will boost the performance when there will be insufficient chemical

passivation of defects. The performance of the CIGS solar cell is not only contributed from the intrinsic inhomogeneity of the stack of the layer but also the various environmental condition exposure. Degradation of a cell or a module is measured in terms of the rate of change in the efficiency of cells or modules over a duration (year) [47]. At cell level and module, degradation occurs at various modes listed as intrinsic degradation in devices like: (1) At main absorber/buffer p-n junction due to diffusion of dopants, impurities, and electromigration, recombination is increased which reduces the short circuit current, open-circuit voltage and fill factor. (2) Shunting in the absorber layer decreases shunts resistance R_{shunt} . (3) Increases in series resistance due to back (Mo) and rear (AZO) corrosion or diffusion leads to degradation. (4) Lamination stress may delaminate Mo back contact and thus reducing the short circuit current. Fabrication of CIGS module possesses degradation mechanisms at interconnection and encapsulation such as (1) corrosion and electromigration increases series resistance and decreases shunt resistance at interconnect of Mo, AZO/Mo, or across isolation during scribing. (2) Failure in busbar or solder increases a series of resistance or they may be open-circuit conditions. (3) Encapsulation delamination, glass breakage or damaging, poor hermetic seal, and loss of high potential at isolation eventuate due to contamination at the surface, the adverse impact of UV exposure hydrolysis of glass bond, warped glass, dinged glass edge, and mismatch of thermal expansion. This results in loss of fill factor, short circuit current and there is probably of open circuit condition. Lifetime and reliability are the two parameters that measure the field performance of the solar cell and module. To measure lifetime and reliability CIGS module must surpass the “Accelerated Lifetime Testing (ALT)” testing procedure and these are according to the “International Electrotechnical Commission (IEC) 61646” standard [48]. This ‘ALT’ standard includes exposure of liquid or gaseous water, heat, and humidity on the cell and module. Several degradation tests are mentioned as (1) standard damp heat exposure (85 °C/85 % RH), (2) mild damp heat (60 °C/90 % RH or 60 °C/60 % RH), (3) dry heat (85-90 °C/10 % RH), (4) combined damp-heat and illumination (85 °C/ 85 RH + UV illumination), (5) thermal cycling (-40 °C (cold) to + 85 °C (warm) temperature shock) and (6) potential induced degradation i.e. application of high

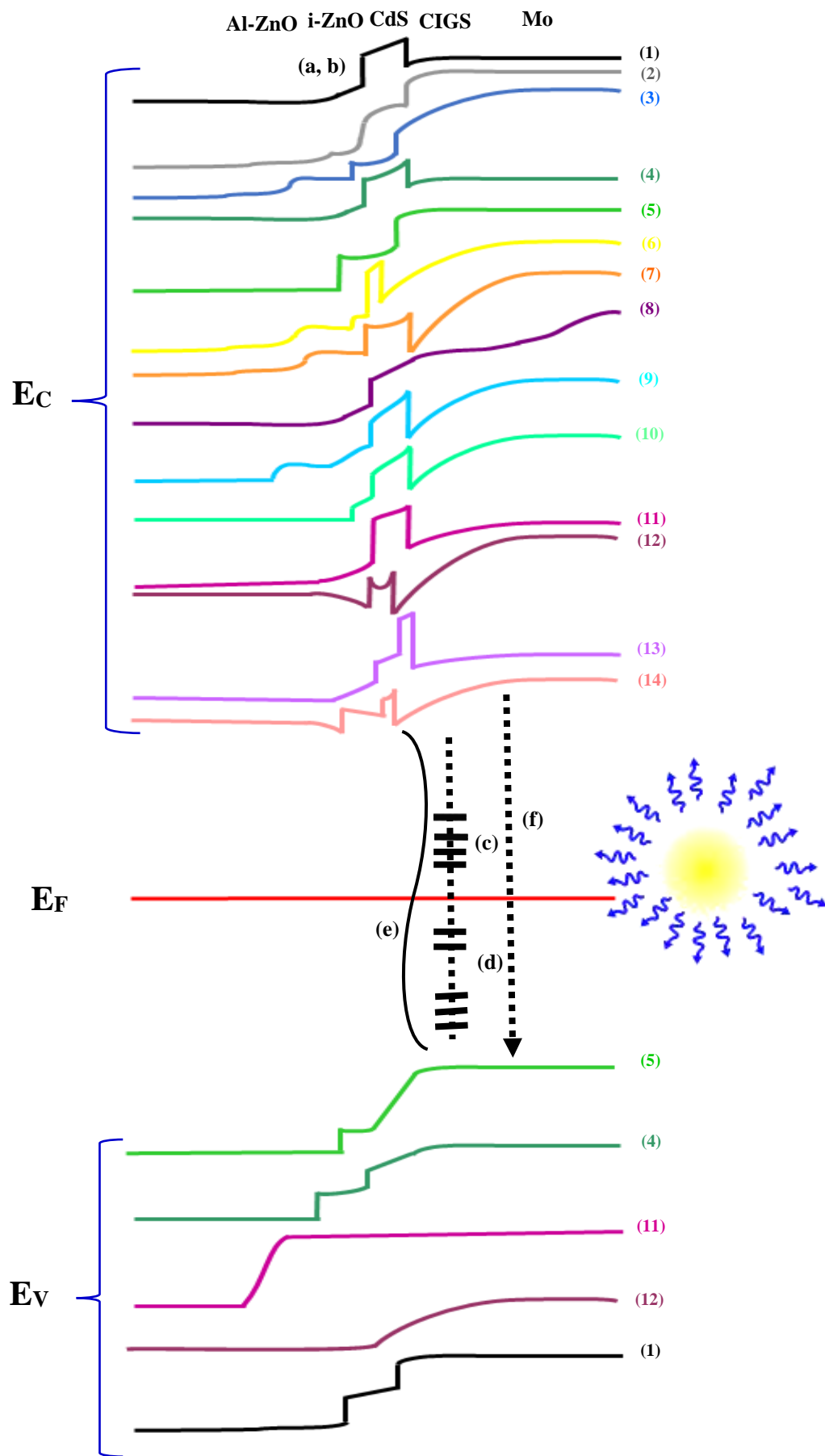


Fig.1.6: Band alignment of CIGS solar cell device having SLG/Mo/CIGS/CdS/i-ZnO/AZnO structure under various deposition parameters. Here ‘E_c’ is the conduction band, ‘E_F’ is Fermi Energy and ‘E_v’ is the valence band. The conduction band and its corresponding valence band are represented by the same numerical notation. Few valence band results are not mentioned here as data is not available in the respective literature. Possible losses in device (a) diffusion, (b) thermionic emission, (c) non-radiative, (d) trap-assisted tunneling, (e) CIGS/CdS interface and (6) radiative at bulk, p-n junction, and interfaces.

voltage to module in both dry and humid environmental condition. Exposure of all different layers of CIGS solar module to ‘ALT’ test conditions results in degradation and poor performance of cells and modules. Initiating with back contact, the Mo layer form the MoO₂/MoO₃ layer which is a poor conductor having blue or black spots when exposed to water and oxygen at elevated temperature. But this MoO₃ converts to MoSe₂ on the deposition of CIGS. An absorber CIGS layer gets deteriorated under damp heat and air exposure. Spots of low concentrated gallium, copper, and selenium whereas sodium with high concentration was observed. This may be due to hydrolysis and oxidation reactions. Presences of water form oxides (In(OH)₃, Ga(OH)₃, H₂SO₃, and NaOH which reduces the carrier lifetime of CIGS and finally degrades it. Buffer layer CdS under damp heat exposure reacts and diffuses into CIGS as well as the ZnO layer and form sulfates such as ZnSO₄, Cd_{1-x}Zn_xS, and ZnO_{1-x}S_x. Inefficacious CdS thickness degrades the CdS/ZnO interface and reduces resistivity and stability of the AZO layer. The AZO layer plays a foremost role in CIGS module stability and degradation. AZO has a high Water Vapor Transmission Rate (WVTR) of 1×10^{-5} g/m²/day. Not only AZO but the i-ZnO layer also has WVTR of 1.3×10^{-5} g/m²/day so it acts as a water barrier layer to the CIGS layer. Moisture, CO₂, and foreign particles from the atmosphere interact with the AZO layer at grain boundaries and precipitates Al(OH)₃, Zn(CO₃), Zn(OH)₂, and Zn₅(CO₃)₂(OH)₆ molecules having low conductivity. These molecules are formed due to molecular adsorption or chemical reaction with the AZO layer and in turn, degrades the performance of CIGS cells and modules. AZO layer exposed to damp heat test decreases the conductivity and

mobility whereas negligible variation was observed for carrier concentration. Also, the low thickness of the AZO layer degrades faster compared to thicker ones. CIGS module has a different degradation scenario compared to cells. Particularly interconnection of scribes gets deteriorated and thus degradation is reflected in the poor performance of the module. P1 scribe forms a shunt path between CIGS and Mo layer after damp heat exposure. In the case of the P2 scribe, Mo and AZO layer interconnection is get affected by damp heat exposure which increases resistivity and hinders the current transport mechanism in the CIGS module. The growth of the oxide layer at Mo/AZO scribe is also one of the causes of P2 degradation. P3 scribe degradation is dominated by the MoO₂ layer due to due corrosion of the Mo layer.

1.7 Organization of thesis

Chapter 1:

A remarkable achievement in the development of photovoltaic cells, technology is presented in this chapter. The current scenario of different photovoltaic devices and road map towards high efficiency is well described. An outline of the role of material properties of Molybdenum, Copper Indium Gallium Diselenide, Cadmium Sulphide, intrinsic-Zinc Oxide, and Aluminum doped Zinc Oxide are well described. The importance and key feature of the glass substrate are also explained in this chapter. Merits and demerits of different types of the interconnection of the solar cell are also summarized.

Chapter 2:

This chapter's deal with a variety of deposition and characterizations techniques used for developing and fabrication of CIGS solar cell module. Structural, optical, electrical, morphology, elemental composition, and thickness properties of the different layers and finally device characteristics have been studied. For this, X-ray diffraction, Optical, Atomic Force Microscopy, Scanning Electron Microscopy, Transmission Electron Microscopy, Vander Pauw method and Four Point Probe method for electrical, Elemental Dispersive X-ray Analysis, Photoluminescence, and Raman Spectroscopy, Current-Voltage (I-V) characteristics were analyzed for detail assessment.

Chapter 3:

An ohmic back contact for CIGS solar cell module was developed using refractory material i. e. Molybdenum (Mo) deposited by DC sputtering. Single, as well as bilayer Mo thin film, was deposited at constant argon flow. For single-layer deposition pressure was varied as 10 and 1 mTorr while for bilayer, a bottom layer at 10 mTorr, and top layer 1 mTorr. Each layer has a 0.5 μm thickness. DC sputter power varied as (50, 100, 150, and 200 W) and two different substrate temperature (Room temperature and ST-215 °C) was kept constant. Structural, optical, electrical, morphological studies were carried out. The adhesion test was tested using mechanical and laser technology. For the monolithic interconnection P1 process was optimized using Nd:YAG 1064 nm laser by varying parameter Viz. (pulse repetition frequency (PRF), power, speed, and pass delay). All the above-mentioned deposition and process parameters were tuned to obtain high reflectivity, low resistive, and highly adhesive back ohmic contact with burr-free clean electrical isolation are reported in this chapter.

Chapter 4:

Single quaternary chalcopyrite Copper Indium Gallium Diselenide (CIGS) sputter target was in-house fabricated using a high energy ball milling technique followed by a vacuum sintering process. Using this sputtering target, CIGS thin films using an RF sputtering technique on a 60 x 60 x 1 mm SLG substrate will be deposited. The influence of RF power, deposition pressure, substrate temperature on physical, optical, electrical properties of CIGS thin film was studied. In addition to it, the annealing process will be done to study the change in properties as well as an increment in grain size and etch out the binary phase. Structural, optical, electrical, elemental composition properties were characterized to optimized CIGS thin film as an absorber layer.

Chapter 5:

Buffer layer was studied using two different techniques i. e., (1) Thermal evaporation and (2) Chemical Bath Deposition (CBD). Cadmium Sulphide

(CdS) is an n-type semiconductor, the material used in p-n junction formation. In chapter 5, both deposition techniques were used to deposit CdS thin film on a 60 x 60 x 1 mm SLG substrate. For thermal evaporation deposition, CdS powder was used and substrate temperature was varied (RT, 100, 125, 150, and 175 °C); for CBD deposition sulfur to cadmium, the ratio was varied as (1, 2.5, 5, and 7). Characterizations such as structural, optical, Urbach energy, light, and dark resistivity, and photoluminescence analysis were carried out to optimize the CdS buffer layer for the development of the CIGS solar module.

Chapter 6:

The top window layer of the solar cell is very active in collecting photons from sunlight. Transparent conductive oxide is the best choice and Aluminum doped zinc oxide is the best candidate for it. In this chapter, the influence of deposition parameter Viz., deposition pressure, RF power, substrate temperature, and thickness on structural, optical, electrical, topographical, and microstructural analysis of AZO thin films and i-ZnO thin films were carried out. In addition to it, structure symmetry and presence of defects, impurities in the presence of variable deposition parameters were also analyzed using Raman and photoluminescence spectroscopic analysis. Both i-ZnO and AZO thin films were sputtered using RF sputtering technique on a 60 x 60 x 1 mm SLG substrate. For an i-ZnO thin film in-house 2-inch (diameter) sputter target was fabricated using ZnO powder (99.9 %) while for AZO thin films AZO sputter target (American Elements) (2 % Al₂O₃) was used.

Chapter 7:

Fabrication of CIGS solar cell module on 60 x 60 x 1 mm SLG substrate was briefly described in this chapter. For developing CIGS solar stack optimized ohmic back contact (Mo), absorber layer (CIGS), buffer layer (CdS), top window layer (i-ZnO, and AZO) was deposited followed by an intermediate laser scribing process for electrical isolation of each solar cell. I-V (open-circuit voltage V_{oc} , short circuit current I_{sc} , fill factor FF, and quantum efficiency η %) characteristics of CIGS thin-film solar module were analyzed for estimating the performance of the solar cell module.

References

- [1] Joshua M. Pearce, *Futures*, **34** (2002) 663–674.
- [2] Shruti Sharma, Kamlesh Kumar Jain, and Ashutosh Sharma, *Materials Sciences and Applications*, **6** (2015) 1145-1155.
- [3] *BP Statistical Review of World Energy*-69th edition, (2020) 1-68.
- [4] www.ibef.org.
- [5] G. N. Tiwari and Arvind Tiwari Shyam, *Handbook of Solar Energy Theory, Analysis and Applications*, Springer Science + Business Media, Singapore (2016).
- [6] C. Riordan and R. Hulstrom, *IEEE Conference on Photovoltaic Specialists*, Kissimmee, FL, USA, **2** (1990) 1085-1088.
- [7] Daryl R. Myers, Keith Emery and C. Gueymard, *ASES/ASME Solar*, Reno, Nevada, NREL/CP-560-32284, (2002) 1-10.
- [8] Martin A. Green, *Nature Energy*, **1** (2016) 23-34.
- [9] W. Zulehner, *J. Cryst. Growth.*, **65** (1983) 189-213.
- [10] J. Benick, A. Richter, R. M'uller, H. Hauser, F. Feldmann, P. Krenckel, S. Riepe, F. Schindler, M. C. Schubert, M. Hermle, A. W. Bett, and S. W. Glunz, *IEEE J. Photovolt.*, **7** (2017) 1171-1175.
- [11] K. Yoshikawa, H. Kawasaki, W. Yoshida, T. Irie, K. Konishi, K. Nakano, T. Uto, D. Adachi, M. Kanematsu, H. Uzu and K. Yamamoto et al., *Nat. Energy.*, **2** (2017) 1-8.
- [12] K. L. Chopra, P. D. Paulson and V. Dutta, *Prog. Photovolt: Res. Appl.*, **12** (2004) 69-92.
- [13] K. Ramanathan, M. A. Contreras, C. L. Perkins, S. Asher, F. S. Hasoon, J. Keane, D. Young, M. Romero, W. Metzger, R. Noufi, J. Ward and A. Duda, *Prog. Photovolt: Res. Appl.*, **11** (2003) 225-230.
- [14] S. J. C. Irvine, V. Barrioz, D. Lamb, E. W. Jones, R. L. Rowlands-Jones, *J. Cryst.*, **310** (2008) 5198-5203.
- [15] S. P. Tobin, S. M. Vernon, C. Bajgar, S. J. Wojtczuk, M. R. Melloch, A. Keshavarzi, T. B. Stellwag, S. Venkatesan, M. S. Lundstrom and K. A. Emery, *IEEE T Electron Dev.*, **37** (1990) 469-477.

- [16] S. Lu, L. Ji, W. He, P. Dai, H. Yang, M. Arimochi, H. Yoshida, S. Uchida and Masao Ikeda, *Nanoscale Res. Lett.*, **6** (2011) 576189-1-576189-4.
- [17] First Solar Press Release, *First Solar builds the highest efficiency thin film PV cell on record*, 5 August 2014, 1-4.
- [18] T. Kato, *JJAP.*, **56** (2017) 04CA02-1-04CA02-8.
- [19] B. M. Kayes, H. Nie, R. Twist, S. G. Spruytte, F. Reinhardt, I. C. Kizilyalli, and G. S. Higashiet, *37th IEEE Photovoltaic Specialists Conference*, (2011).
- [20] Martin A. Green, Ewan D. Dunlop, Jochen Hohl-Ebinger, Masahiro Yoshita, Nikos Kopidakis and Xiaojing Hao, *Prog Photovolt Res Appl.*, version **57** (2020) 1-13.
- [21] V. Fthenakis, *Renew. Sustain. Energy Rev.*, **13** (2009) 2746-2750.
- [22] J. Yan and B. R. Saunders, *RSC. Adv.*, **4** (2014) 43286-43314.
- [23] M. Yamaguchi, L. Zhu, H. Akiyama, Y. Kanemitsu, H. Tampo, H. Shibata, Kan-Hua Lee, K. Araki, and N. Kojima, *JJAP.*, **57** (2018) 04FS03-1-04FS03-6.
- [24] R. Søndergaard, M. Hösel, D. Angmo, T. T. Larsen-Olsen, and F. C. Krebs, *Mater. Today.*, **15** (2012) 36-49.
- [25] M. Mokhtarimehr, I. Forbes, and N. Pearsall, *JJAP.*, **57** (2018) 08RC14-1-08RC14-6.
- [26] N. Kato, S. Moribe, M. Shiozawa, R. Suzuki, K. Higuchi, A. Suzuki, M. Sreenivasu, K. Tsuchimoto, K. Tatematsu, K. Mizumoto, S. Doi and T. Toyoda, *J. Mater. Chem. A*, **6** (2018) 22508-22512.
- [27] C. Yan, J. Huang, K. Sun, S. Johnston, Y. Zhang, H. Sun, A. Pu, M. He, F. Liu, K. Eder, L. Yang, J. M. Cairney, N. J. Ekins-Daukes, Z. Hameiri, J. A. Stride, S. Chen, M. A. Green, and X. Hao, *Nat. Energy.*, **3** (2018) 764-772.
- [28] https://www.toshiba.co.jp/rdc/rd/detail_e/e1407_02.html.
- [29] W. Shockley and H. J. Queisser, *J. Appl. Phys.*, **32** (1961) 510-519.
- [30] Daniel Abou-Ras, Thomas Kirchartz, and Uwe Rau, *Advanced Characterization Techniques for Thin Film Solar Cells*, WILEY-VCH Verlag GmbH & Co. KGaA, Boschstr (2011).

- [31] Fadong Yan, David J. Metacarpa, R. Sundaramoorthy, Dave Fobare, and Pradeep Haldar, *IEEE 39th Photovoltaic Specialists Conference (PVSC)*, Tampa, FL, (2013).
- [32] B. J. Stanbery, *Critical Reviews in Solid State and Materials Sciences*, **27(2)** (2002) 73-117.
- [33] E. Handick, P. Reinhard, R. G. Wilks, F. Pianezzi, T. Kunze, D. Kreikemeyer-Lorenzo, L. Weinhardt, M. Blum, W. Yang, M. Gorgoi, E. Ikenaga, D. Gerlach, S. Ueda, Y. Yamashita, T. Chikyow, C. Heske, S. Buecheler, A. N. Tiwari, and M. Baer, *ACS Appl. Mater. Interfaces*, **9** (2017) 3581-3589.
- [34] S. Karki, P. Paul, G. Rajan, B. Belfore, D. Poudel, A. Rockett, E. Danilov, F. Castellano, A. Arehart, and S. Marsillac, *IEEE Journal of Photovoltaics*, **9** (2019) 313-318.
- [35] K. A. Jones, *J. Cryst. Growth*, **47**(1979) 235-244.
- [36] D. Schmid, M. Ruckh and H. W. Schock, *Sol. Energy Mater Sol.*, **41/42** (1996) 281-294.
- [37] Md. Asaduzzaman, Md. Billal Hosen, Md. Karamot Ali, and Ali Newaz Bahar, *Int J Photoenergy*, **2017** (2017) 1-8.
- [38] Roy G. Gordon, *MRS BULLETIN* **25(8)** (2000) 52-57.
- [39] A. Lemke, D. Ashkenasi and H. J. Eichler, *Physics Procedia*, **41** (2013) 769-775.
- [40] J. F. Guillemoles, L. Kronik, D. Cahen, U. Rau, A. Jasenek, and H. W. Schock, *J. Phys. Chem. B*, **104** (2000) 4849-4862.
- [41] S. H. Wei and A. Zunger, *Appl. Phys. Lett.*, **63** (1993) 2549-2551.
- [42] A. O. Pudov, A. Kanevce, H. A. Al. Thani, J. R. Sites, and F. S. Hasoon, *J. Appl. Phys.*, **97** (2005) 064901-6.
- [43] Y. Sun, S. Lin, W. Li, S. Cheng, Y. Zhang, Y. Liu and W. Liu, *Engineering*, **3** (2017) 452-459.
- [44] O. Lundberg, M. Edoff and L. Stolt, *Thin Solid Films*, **480-481** (2005) 520-525.
- [45] F. Larsson, J. Keller, M. Edoff and T. Törndahl, *Thin Solid Films*, **633** (2017) 235-238.

- [46] G. Sozzi, S. D. Napoli, R. Menozzi, B. Bissig, S. Buecheler and A. N. Tiwari, *Sol. Energy Mater Sol.* **165** (2017) 94-102.
- [47] M. Theelen and F. Daume, *J. Sol. Energy*, **133** (2016) 586-627.